

Application of cross correlations between CMB and large scale structure to constraints on the primordial non-Gaussianity

Yoshitaka Takeuchi,^{1,*} Kiyotomo Ichiki,^{1,†} and Takahiko Matsubara^{2,‡}

¹*Department of Physics, Nagoya University, Chikusa-ku, Nagoya, 464-8602, Japan*

²*Kobayashi-Maskawa Institute for the Origin of Particles and the Universe,
Nagoya University, Chikusa-ku, Nagoya, 464-8602, Japan*

(Dated: October 23, 2018)

The primordial non-Gaussianity of local type affects the clustering of dark matter halos, and the planned deep and wide photometric surveys are suitable for examining this class of non-Gaussianity. In our previous paper, we investigated the constraint from the cross correlation between CMB lensing potential and galaxy angular distribution on the primordial non-Gaussianity, without taking into account redshift slicing. To improve our previous analysis, in this paper, we add the galaxy lensing shear into our analysis and take into account redshift slicing to follow the redshift evolution of the clustering. By calculating 81 power spectra and using the Fisher matrix method, we find that the constraint on the primordial non-Gaussianity can be improved from $\Delta f_{\text{NL}} \sim 5.4$ to 5.1 by including the galaxy-galaxy lensing shear cross correlations expected from the Hyper Suprime-Cam survey (HSC), in comparison with the constraint without any cross correlations. Moreover, the constraint can go down to $\Delta f_{\text{NL}} \sim 4.8$ by including the galaxy-CMB lensing cross correlations from the ACTPol and Planck experiments.

PACS numbers: 98.80.-k, 98.62.Sb, 98.65.-r

I. INTRODUCTION

Primordial non-Gaussianities have been intensively discussed, because any detection of them offers an important window into the early Universe. Standard single-field slow-roll inflation models predict small non-Gaussianity [1–5], so that the detection of large non-Gaussianity may turn down the standard model and suggest physics beyond the standard model. The most popular method to hunt for primordial non-Gaussianities is to measure higher order correlation functions of the cosmic microwave background (CMB) anisotropies such as the three-point correlation function (bispectrum) and the four-point one (trispectrum). Non-vanishing signals of these higher order correlations may predict the presence of primordial non-Gaussianities. [6–11].

Recently, many studies have revealed that the primordial non-Gaussianity of local type affects the large-scale structure (LSS) through the clustering of dark matter halos, and shown the modification of the halo mass function [12–17] and the halo bias [18–24], both by numerical simulations and by analytic calculations. Among several types of primordial non-Gaussianities, the local-type non-Gaussianity induces strong scale-dependence of the halo bias [18–21]. This scale-dependent bias is also powerful tool to constrain the primordial non-Gaussianity from the observations of LSS independently of the method with CMB higher order correlation functions.

Using this scale-dependent feature in the halo bias, some measurements of the primordial non-Gaussianity have been done in Refs. [18, 20, 25]. It is expected that future wide and deep surveys, such as Subaru Hyper Suprime-Cam (HSC) survey [26], Dark Energy Survey (DES) [27], Large Synoptic Survey Telescope (LSST) [28], and so on, will put tighter constraints on the primordial non-Gaussianity, which are expected to be comparable to those from the future CMB observations or more (e.g., [29–32]).

To get a tighter constraint on the primordial non-Gaussianity, it is important to distinguish the signature of the primordial non-Gaussianity from the other effects more precisely, especially from the linear bias in the limited survey area. Thus, it is better for this purpose to combine unbiased observables which are sensitive to the matter power spectrum in the near Universe, such as weak gravitational lensing of CMB and galaxy lensing shear.

Cross correlations with complementary probes are expected to provide additional information on top of their respective auto correlations. The cross correlation between CMB and LSS is known to give information about the integrated Sachs-Wolfe (ISW) effect of CMB temperature anisotropy, which generates the secondary anisotropies due to the time variation of the gravitational potential [33]. Moreover, CMB lensing also has a correlation with LSS since the gravitational lensing of CMB is induced by the gravitational potential produced by LSS, and the galaxy lensing shear as well [34].

Since the effects of the CMB lensing are imprinted on small scales, the Wilkinson Microwave Anisotropy Probe (WMAP) satellite has not detected the CMB lensing directly. Recent ground based CMB experiments such as Atacama Cosmology Telescope (ACT), announced the

*Electronic address: yositaka@phys.nagoya-u.ac.jp

†Electronic address: ichiki@phys.nagoya-u.ac.jp

‡Electronic address: taka@phys.nagoya-u.ac.jp

detection of the CMB lensing signal, and an ongoing CMB observation by Planck [35] or various ground based experiments are expected to detect this signal more precisely. Therefore, we can be sure that the observation of CMB lensing will increase its accuracy and play an important role in observational cosmology in near future surveys.

In this paper we consider prospects for constraining the primordial non-Gaussianity through the scale-dependent bias from the near future surveys taking into account all auto and cross correlations among CMB, galaxy distribution and galaxy lensing shear. We shall show that galaxy-CMB lensing and galaxy-galaxy lensing cross correlations are particularly fruitful and allow us to improve the constraints on the primordial non-Gaussianity.

This paper is organized as follows. In section II we briefly review the effects of the primordial non-Gaussianity for large-scale structure and show the modifications to the mass function and bias of dark matter halos. In section III we summarize the observables employed in our analysis and describe the angular power spectra of the cross correlations between CMB and LSS. In section IV we mention the survey design and photometric redshift systematics employed in our analysis. In section V we explain the method and the setup of our analysis. In section VI we show the results particularly focusing on the constraints on the primordial non-Gaussianity. In section VII we discuss the effects of the photometric redshift systematics and the massive neutrino on the constraints. Then we assess the contribution of the cross correlations for the constraints. Moreover, we compare the constraints from some different surveys. Finally, in section VIII we summarize our conclusions. Through this paper we assume a spatially flat Universe for simplicity.

II. PRIMORDIAL NON-GAUSSIANITY

Deviations from Gaussian initial conditions are commonly parameterized in terms of the dimensionless parameter f_{NL} and the primordial non-Gaussianity of the local form is described as [3, 36, 37]

$$\Phi = \phi + f_{\text{NL}}(\phi^2 - \langle \phi^2 \rangle), \quad (1)$$

where Φ is the curvature perturbation and ϕ is a Gaussian random field. On the subhorizon scale, Φ is related to the Newtonian gravitational potential Ψ as $\Phi = -\Psi$.

The existence of the primordial non-Gaussianity, $f_{\text{NL}} \neq 0$, indicates that the initial density field is positively or negatively skewed. Furthermore, the fact that the non-Gaussianity affects the clustering of dark matter halos or galaxies allows us to constrain on the non-Gaussianity from large-scale structure surveys. In particular, the local-type non-Gaussianity described by Eq. (1) induces a scale-dependent enhancement of the halo/galaxy power spectrum.

In the presence of the primordial non-Gaussianity, the mass function of clustering halos is modified and we adopt a non-Gaussian correction factor of the halo mass function based on the Edgeworth expansion [12]:

$$\frac{dn/dM}{dn_{\text{G}}/dM} = 1 + \frac{\sigma_M S_3}{6}(\nu^2 - 3\nu) - \frac{1}{6} \frac{d(\sigma_M S_3)}{d \ln \nu} \left(\nu - \frac{1}{\nu} \right), \quad (2)$$

where S_3 is the skewness of the density field which is proportional to f_{NL} , $\sigma_M = \sigma_M(M, z)$ is the rms of the linear density field smoothed on mass scale M , ν is defined as $\nu = \delta_c/\sigma_M$ and $\delta_c \sim 1.68$ is the critical linear overdensity. dn/dM is the mass function in the non-Gaussian case and dn_{G}/dM is the one in the Gaussian case. For the Gaussian one, we adopt a model of Warren *et al* [38].

Recent studies have shown that the local-type primordial non-Gaussianity produces a scale-dependent enhancement of the clustering of halo on large-scales,

$$P_{\text{g}}(M, z, k) = b_{\text{G}}^2(M, z)P(k, z) \rightarrow [b_{\text{G}} + \Delta b(M, z, k)]^2 P(k, z), \quad (3)$$

where $P_{\text{g}}(M, z, k)$ is the galaxy power spectrum, $P(k, z)$ is the matter power spectrum, $b_{\text{G}}(M, z)$ is the bias in the Gaussian case and $\Delta b(M, z, k)$ is the non-Gaussian correction of the halo bias described as [24]

$$\Delta b(M, z, k) = \frac{3\Omega_{\text{m},0}H_0^2}{k^2 T(k)D(z)} f_{\text{NL}} \delta_c (b_{\text{G}}(M, z) - 1) - \frac{\nu}{\delta_c} \frac{d}{d\nu} \left(\frac{dn/dM}{dn_{\text{G}}/dM} \right). \quad (4)$$

Here, $\Omega_{\text{m},0}$ and H_0 are the matter energy density normalized by the critical density and the Hubble parameter at present, $D(z)$ is the linear growth rate normalized to the scale factor a in the matter-dominant era and $T(k)$ is the transfer function of linear matter density fluctuations. For the halo bias in the Gaussian case $b_{\text{G}}(M, z)$, we assumed the form presented by Sheth *et al* [39].

III. ANGULAR POWER SPECTRUM

Here we briefly review the auto and cross correlations of various cosmological observables and their angular power spectra. In this paper we take into account CMB temperature (T) anisotropies, E -mode polarization (E) and CMB lensing potential (ψ) for CMB observables and galaxy distribution (g) and weak lensing shear (γ) for LSS observables.

A. Integrated Sachs-Wolfe (ISW) effect

The decay of the Newtonian potential due to the presence of dark energy produces a differential gravitational redshift, and this effect is called the late-time integrated Sachs-Wolfe (ISW) effect. In a flat Universe the presence of ISW effect is a signature of dark energy, and induces

a non-vanishing cross correlation between CMB temperature and large-scale structure measurements, such as galaxy distribution, weak lensing field and so on.

The contribution of the ISW effect to the CMB temperature field $\Theta(\hat{\mathbf{n}})$ can be written as

$$\Theta_{\text{ISW}}(\hat{\mathbf{n}}) = \frac{\Delta T_{\text{ISW}}(\hat{\mathbf{n}})}{T_{\text{CMB}}} = -\frac{2}{T_{\text{CMB}}} \int_0^{\chi_*} d\chi \dot{\Phi}(\chi \hat{\mathbf{n}}, \chi), \quad (5)$$

where T_{CMB} is the mean temperature of the CMB, $\hat{\mathbf{n}}$ is the direction to the line of sight, χ is the comoving distance and χ_* denotes the distance to the last scattering surface. $\dot{\Phi}$ is the gravitational potential and a dot denotes a derivative with respect to the conformal time.

The angular power spectrum of the cross correlation between CMB temperature through ISW effect and the other measurements X can be written as

$$C_\ell^{TX} = \frac{2}{\pi} \int k^2 dk P_\Phi(k) \Delta_\ell^{\text{ISW}}(k) \Delta_\ell^X(k), \quad (6)$$

where

$$\Delta_\ell^{\text{ISW}}(k) = 3\Omega_{\text{m},0} H_0^2 \int_0^{z_*} dz \frac{d}{dz} \left\{ \frac{D(z)}{a(z)} \right\} T(k) j_\ell(k\chi(z)), \quad (7)$$

$P_\Phi(k) \propto k^{n^s-4}$ is the primordial power spectrum of Φ as a function of the wave number k and n^s is the tilt of the primordial power spectrum. The functions $T(k)$ and $D(z)$ are the transfer function and the growth rate for linear matter density fluctuations, respectively, and $j_\ell(k\chi)$ is a spherical Bessel function. The kernel $\Delta_\ell^X(k)$ is for the other measurements, namely, CMB lensing potential, galaxy distribution and weak lensing shear in this paper; $X = \psi, g, \gamma$, respectively.

The noise spectra of CMB include detector noise and residual foreground contamination. Here, we assume the ideal condition that foreground contamination can be completely removable and include only Gaussian random detector noise of the form [40]

$$N_\ell^{T,P} = \left[\sum_\nu \left\{ (\theta_{\text{FWHM}} \Delta_{T,P})^{-2} e^{-\ell(\ell+1)\theta_{\text{FWHM}}/8 \ln 2} \right\} \right]^{-1}, \quad (8)$$

where θ_{FWHM} is the spatial resolution of the beam and $\Delta_{T,P}$ represents the sensitivity to the temperature and polarization per pixel, respectively. These values are given for each of the frequency bands of channels ν and we show the values for two CMB experiments such as Planck [35] and ACT with new polarization sensitive receiver (ACTPol) [41] in Table I.

B. CMB lensing potential

CMB photons are deflected due to the gravitational potential produced by the large-scale structure on the way propagating to us (e.g., Ref. [42]). The relationship between the lensed temperature anisotropy $\tilde{T}(\hat{\mathbf{n}})$ and the

experiment	f_{sky}	ν [GHz]	θ_{FWHM} [arcmin]	Δ_T [$\mu\text{K}/\text{pixel}$]	Δ_P [$\mu\text{K}/\text{pixel}$]
Planck	0.65	100	9.5'	6.8	10.9
		143	7.1'	6.0	11.4
		217	5.0'	13.1	26.7
ACTPol	0.05	148	1.4'	3.6	5.0

TABLE I: The specifications for CMB experiments. f_{sky} is the sky coverage, θ_{FWHM} is the beam width at FWHM, Δ_T and Δ_P represent the sensitivity of each channel to the temperature and polarization, respectively, and ν means the channel frequency.

unlensed one $T(\hat{\mathbf{n}})$ is given by the deflection angle $\mathbf{d}(\hat{\mathbf{n}})$ as $\tilde{T}(\hat{\mathbf{n}}) = T(\hat{\mathbf{n}} + \mathbf{d})$. The deflection is related to the line of sight projection of the gravitational potential $\Psi(\hat{\mathbf{n}}, z)$ as $\mathbf{d}(\hat{\mathbf{n}}) = \nabla\psi(\hat{\mathbf{n}})$, where

$$\psi(\hat{\mathbf{n}}) = -2 \int_0^{\chi_*} d\chi \frac{\chi_* - \chi}{\chi_* \chi} \Psi(\chi \hat{\mathbf{n}}, \chi). \quad (9)$$

Here, $\psi(\hat{\mathbf{n}})$ is the (effective) lensing potential.

The angular power spectrum of the lensing potential can be written as

$$C_\ell^\psi = \frac{2}{\pi} \int k^2 dk P_\Phi(k) [\Delta_\ell^\psi(k)]^2, \quad (10)$$

where

$$\Delta_\ell^\psi(k) = 3\Omega_{\text{m},0} H_0^2 \int_0^{\chi_*} d\chi \frac{\chi_* - \chi}{\chi_* \chi} \frac{T(k)D(z(\chi))}{a(\chi)} j_\ell(k\chi). \quad (11)$$

The lensing potential can be reconstructed with quadratic statistics in the temperature and polarization data that are optimized to extract the lensing signal. To reconstruct the lensing potential, one needs to use the non-Gaussian nature imprinted into the lensed CMB statistics, and the noise of the lensing potential can be estimated as the reconstruction error [43, 44]. In this paper, we estimate the noise spectrum of lensing potential N_ℓ^ψ following the technique developed in [44] optimally combining the temperature and polarization fields.

C. Galaxy distribution

The luminous sources such as galaxies must be the most obvious tracers of the large-scale structure in the linear regime, and the projected density contrast of the galaxies can be written as

$$\delta_{\text{g},i}(\hat{\mathbf{n}}) = \int_0^\infty dz b_{\text{eff}}(z, k) \frac{n_i(z)}{n_i^\Lambda} \delta(\chi(z)\hat{\mathbf{n}}, z), \quad (12)$$

where the subscript i represents the i -th redshift bin. $\delta(\chi\hat{\mathbf{n}}, z)$ represents the matter density fluctuation, and $n_i(z)$ and n_i^Λ are the galaxy redshift distribution and the

total number of galaxies per steradian in the i -th redshift bin. The function $b_{\text{eff}}(z, k)$ is the weighted effective halo/galaxy bias defined as

$$b_{\text{eff}}(z, k) = \left[\int_{M_{\text{obs}}}^{\infty} dM \frac{dn}{dM} \right]^{-1} \int_{M_{\text{obs}}}^{\infty} dM b(M, z, k) \frac{dn}{dM}, \quad (13)$$

where M_{obs} is the observable mass threshold, which is the minimum mass of the galaxy we can observe, and we take the value to be $M_{\text{obs}} = 10^{11.7} [h^{-1} M_{\odot}]$. The function $b(M, z, k)$ and dn/dM are the halo mass function and the halo bias in the case of the non-Gaussian initial condition defined in Eqs. (2) and (3), respectively. We show the dependence of $b_{\text{eff}}(z, k)$ on the redshift and the wave number with different mass thresholds and f_{NL} in Fig. 1.

The angular power spectrum of the galaxy distribution between i -th and j -th redshift bins can be written as

$$C_{\ell}^{\text{g}i\text{g}j} = \frac{2}{\pi} \int k^2 dk P_{\Phi}(k) \Delta_{\ell}^{\text{g}i}(k) \Delta_{\ell}^{\text{g}j}(k), \quad (14)$$

where

$$\Delta_{\ell}^{\text{g}i}(k) = \int dz b_{\text{eff}}(z, k) \frac{n_i(z)}{n_i^{\text{A}}} T(k) D(z) j_{\ell}(k\chi). \quad (15)$$

To estimate the signal-to-noise ratios and errors in parameter determination for each survey, we need to describe the noise contribution due to the finiteness in the number of sources associated with source samples. We can write the noise spectra from the shot noise as

$$N_{\ell}^{\text{g}i\text{g}j} = \delta_{ij} \frac{1}{\bar{n}_i}, \quad (16)$$

where \bar{n}_i is the mean surface density of sources per steradian in the i -th redshift bin.

D. Weak lensing shear

The weak lensing shear (equivalently the convergence in the weak lensing limit) is a weighted integral of the density field of sources, which is directly related to the source galaxy redshift distribution. The average convergence of a light ray bundle from sources in the i -th redshift bin is written as

$$\kappa_i(\hat{\mathbf{n}}) = \int_0^{\infty} d\chi W_i(\chi) \delta(\chi \hat{\mathbf{n}}, \chi), \quad (17)$$

where $W_i(\chi)$ is the convergence weight function of kernel defined as

$$W_i(\chi(z)) = \frac{3\Omega_{\text{m},0} H_0^2}{2} \frac{\chi(z)}{a(z)} \int_z^{\infty} dz' \frac{n_i(z')}{n_i^{\text{A}}} \frac{\chi(z') - \chi(z)}{\chi(z')}. \quad (18)$$

Here $\chi(z)$ is the distance to the lens and $\chi(z')$ is the one to the source.

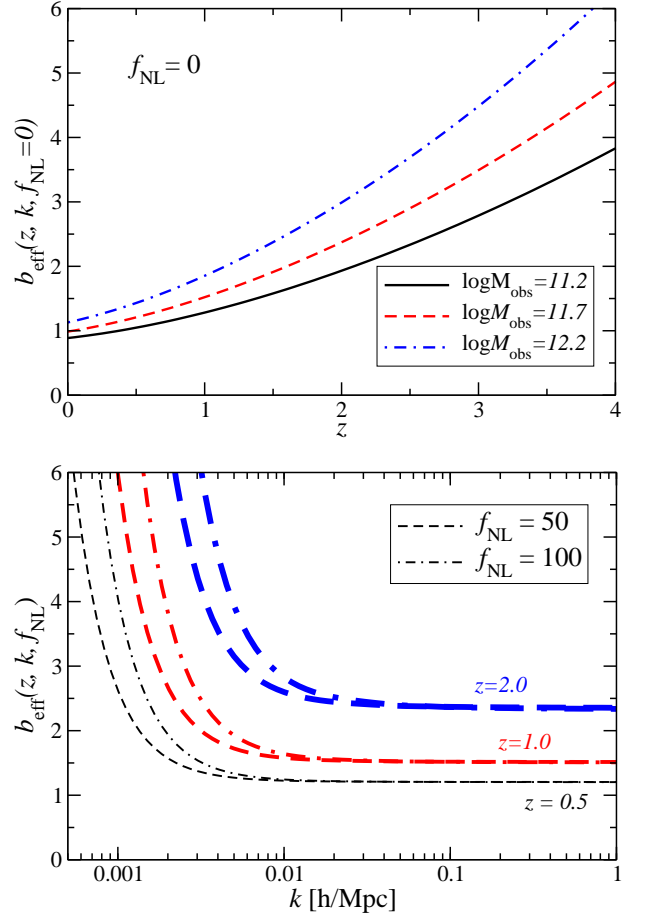


FIG. 1: The effective weighted bias defined in Eq. (13) as a function of redshift z (Top) and as a function of wave number k (Bottom). (Top) We plot the Gaussian case ($f_{\text{NL}} = 0$) for the values $\log M_{\text{obs}} = 11.2, 11.7, 12.2$, respectively, and the k dependence does not appear in this case. (Bottom) We plot the non-Gaussian case ($f_{\text{NL}} = 50, 100$) at redshift $z = 0.5, 1.0, 2.0$ as indicated, and the value $\log M_{\text{obs}}$ is fixed to be $\log M_{\text{obs}} = 11.7$.

The angular power spectra of the weak lensing shear between i -th and j -th redshift bins can be written as

$$C_{\ell}^{\gamma i \gamma j} = \frac{2}{\pi} \int k^2 dk P_{\Phi}(k) \Delta_{\ell}^{\gamma i}(k) \Delta_{\ell}^{\gamma j}(k), \quad (19)$$

where

$$\Delta_{\ell}^{\gamma i}(k) = \int dz W_i(z) T(k) D(z) j_{\ell}(k\chi). \quad (20)$$

The measurement of the shear from galaxy images has some uncertainties, one of which mainly comes from the intrinsic shape ellipticities of galaxies. The galaxy shapes can be treated statistically through a shape noise contribution and the noise spectra can be written as

$$N_{\ell}^{\gamma i \gamma j} = \delta_{ij} \frac{\sigma_{\gamma}^2}{\bar{n}_i}, \quad (21)$$

where σ_γ is the intrinsic galaxy shear. In this paper, we assume the intrinsic galaxy shear to be $\sigma_\gamma = 0.3$ as the

empirically derived value [45] for all surveys.

survey	z_m	\bar{n}_g [arcmin $^{-2}$]	survey area	
DES	0.8	10	5,000 deg 2	($f_{\text{sky}} \simeq 0.12$)
HSC	1.0	30	2,000 deg 2	($f_{\text{sky}} \simeq 0.05$)
LSST	1.2	50	20,000 deg 2	($f_{\text{sky}} \simeq 0.50$)

TABLE II: Survey parameters adopted in this paper for DES, HSC and LSST. The parameter z_m denotes the mean redshift. The parameter \bar{n}_g denotes the mean number density of source galaxies at all redshifts, where the source galaxies are divided into five redshift bins in all surveys. The ranges of redshift are summarized in Table III.

i -th bin	1st	2nd	3rd	4th	5th
redshift range	$0 < z \leq \frac{2}{5}z_m$	$\frac{2}{5}z_m < z \leq \frac{4}{5}z_m$	$\frac{4}{5}z_m < z \leq \frac{6}{5}z_m$	$\frac{6}{5}z_m < z \leq \frac{8}{5}z_m$	$\frac{8}{5}z_m < z \leq z_{\text{max}}$

TABLE III: The redshift ranges of the i -th bin in the case of dividing into five redshift bins. z_m is the mean redshift for each survey shown in Table II. We assume five redshift bins and adopt these redshift ranges for all surveys. z_{max} is the limitation of observations and we assume $z_{\text{max}} = 4.0$ for all surveys in this paper.

E. Cross correlation angular power spectrum

The effect of the primordial non-Gaussianity stands out the most in the galaxy-galaxy auto correlation (gg) through the bias parameter. As many previous works show, almost all the constraints on the primordial non-Gaussianity come from the galaxy-galaxy power spectrum [18, 20, 25, 46, 47]. The cross correlation power spectra, e.g., CMB Temperature-galaxy cross correlation (Tg), however, provide extra information and improve the errors of the parameters.

In our previous analysis [48], we paid a particular attention to the CMB lensing-galaxy cross correlation (ψg), and estimated the contribution to the constraint on the primordial non-Gaussianity. Here, we improve our analysis by adding the galaxy lensing shear, which may also correlated with galaxy distribution and CMB lensing, and estimate the errors of determining cosmological parameters including any possible auto and cross correlations.

Fig. 2 shows an example of the cross correlation angular power spectra, for galaxy-galaxy lensing ($g\gamma$), galaxy-CMB lensing ($g\psi$) and CMB lensing-galaxy lensing ($\psi\gamma$). The boxes around the curve show the expected measurement errors for HSC-like survey (for an illustrating purpose, we take the logarithmic binning, as $\Delta\ell \simeq 0.23\ell$). For the cross correlations with CMB lensing, we show the errors for two cases that one is for Planck and the other is Planck with ACTPol.

IV. SURVEY DESIGN

The errors in determining cosmological parameters from observations of LSS depend a great deal on the survey design, such as the survey region, the mean redshift and photometric redshift errors. Here we summarize the survey design employed in our analysis.

A. Redshift distribution of galaxies

We assume the redshift distribution of galaxy samples with a function of the form:

$$n(z) = \bar{n}_g \frac{\beta}{\Gamma[(\alpha + 1)/\beta]} \frac{z^\alpha}{z_0^{\alpha+1}} \exp \left[- \left(\frac{z}{z_0} \right)^\beta \right], \quad (22)$$

where \bar{n}_g is the mean number density of source galaxies at all redshifts, α , β and z_0 are free parameters. We adopt $\alpha = 2.0$, $\beta = 1.5$, and the parameter z_0 is related to the mean redshift z_m as

$$z_m = \int dz z \frac{n(z)}{\bar{n}_g} = z_0 \frac{\Gamma[(\alpha + 2)/\beta]}{\Gamma[(\alpha + 1)/\beta]}, \quad (23)$$

and z_0 is determined in such a way that the mean redshift z_m fits the value in Table II for each survey. The normalization of the redshift distribution function is fixed by the total number density of galaxies:

$$n^A = \int_0^\infty dz n(z). \quad (24)$$

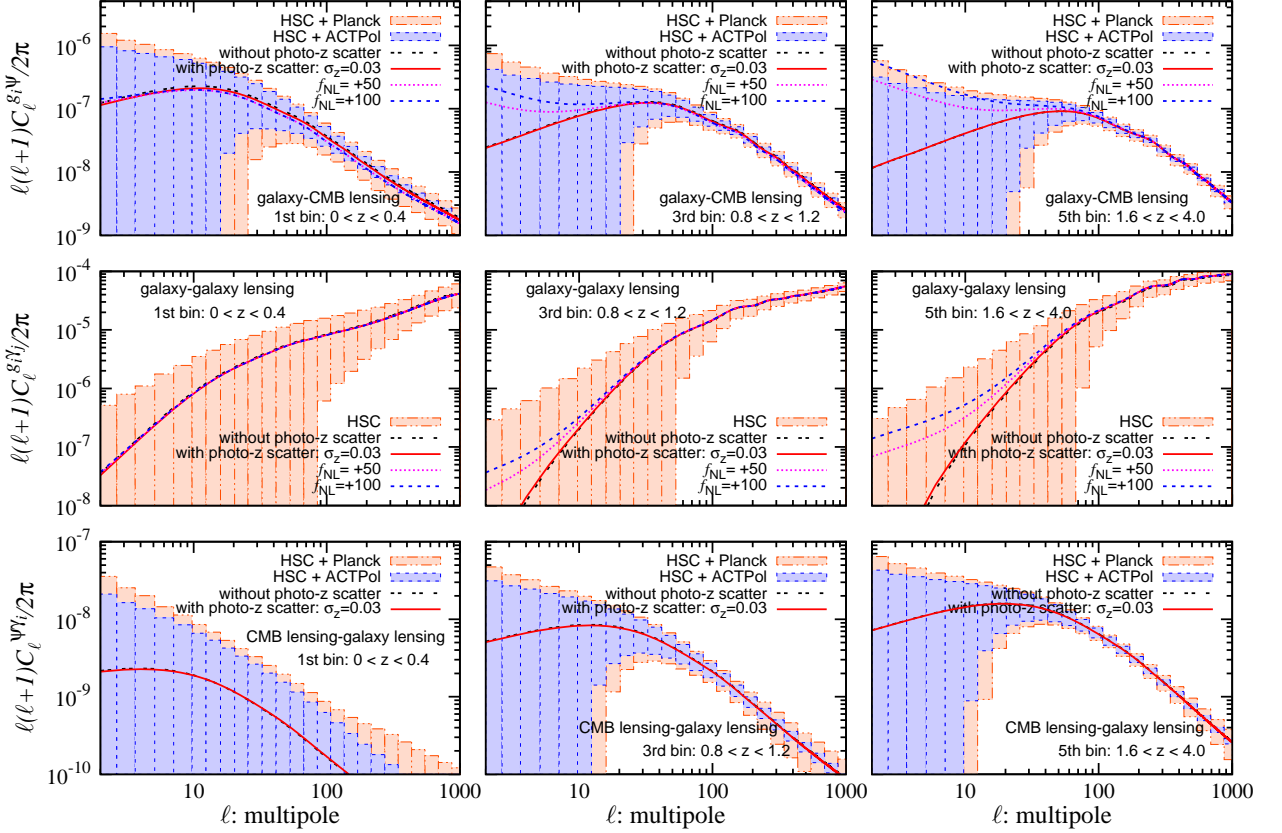


FIG. 2: The angular power spectra for galaxy-CMB lensing ($g_i\psi$; Top), galaxy-galaxy lensing ($g_i\gamma_j$; Middle), and CMB lensing-galaxy lensing ($\psi\gamma_i$; Bottom). Here the subscripts i, j represent the redshift bin and we divided into 5 redshift bins for galaxy distribution (g) and cosmic shear (γ). The angular power spectra shown here are $i = j = 1, 3, 5$ from left to right, respectively. The boxed bars are the errors of the power spectra assuming HSC, Planck and/or ACTPol, and we adopt the logarithmic binning for illustrative purpose. We also plot the angular power spectra in the non-Gaussian case, $f_{\text{NL}} = 50, 100$ and $M_{\text{obs}}[h^{-1}M_{\odot}] = 10^{11.2}, 10^{12.2}$. For comparison, we plot the contribution of the photo- z error, $\sigma_z^{(i)} = 0.03$ for each bin.

B. Photometric redshift systematics

In the galaxy imaging survey whose observables are galaxy distribution and galaxy shear, we measure a large number of galaxies so that the systematic uncertainties play a correspondingly important role with statistical errors. Although systematics may include many effects and these effects depend on the details of the observations [49, 50], we include only the effect of photometric redshift errors.

Imperfect calibration of photometric redshifts induces a residual scatter and bias with respect to the true redshifts, and uncertainties in the redshifts distort the volume element. Following the photometric redshift model as described in [51], the probability distribution of photometric redshift z_{ph} given the true redshift z , $p(z_{\text{ph}}|z)$ is modeled as a Gaussian distribution

$$p(z_{\text{ph}}|z) = \frac{1}{\sqrt{2\pi}\sigma_z} \exp\left[-\frac{(z - z_{\text{ph}} - z_{\text{bias}})^2}{2\sigma_z^2}\right], \quad (25)$$

where $\sigma_z(z)$ and $z_{\text{bias}}(z)$ are the scatter and bias, respectively, which are arbitrary function of redshift z .

The best-estimated distribution for objects in the i -th photometric redshift bin with $z_{\text{ph}}^{(i)} < z < z_{\text{ph}}^{(i+1)}$, $n_i(z)$, can be written as

$$\begin{aligned} n_i(z) &= \int_{z_{\text{ph}}^{(i)}}^{z_{\text{ph}}^{(i+1)}} dz_{\text{ph}} n(z) p(z_{\text{ph}}|z), \\ &= \frac{1}{2} n(z) [\text{erf}(x_{i+1}) - \text{erf}(x_i)], \end{aligned} \quad (26)$$

where x_i is defined as

$$x_i \equiv \left(z_{\text{ph}}^{(i)} - z + z_{\text{bias}}(z)\right) / \sqrt{2}\sigma_z(z). \quad (27)$$

In the same way as Eq. (24), the total number density of galaxies in the i -th bin becomes

$$n_i^A = \int_0^\infty dz n_i(z). \quad (28)$$

We assume a fiducial redshift scatter and bias following [50] as

$$\sigma_z(z) = \sigma_z^{(i)}(1+z), \quad (29)$$

$$z_{\text{bias}}(z) = z_{\text{bias}}^{(i)}(1+z), \quad (30)$$

where $\sigma_z^{(i)}$ and $z_{\text{bias}}^{(i)}$ are defined for each redshift bin. We set the fiducial values as $\sigma_z^{(i)} = 0.03$, $z_{\text{bias}}^{(i)} = 0$ for each redshift bin and all surveys.

V. FORECASTS

We estimate the parameter errors using the Fisher matrix formalism. We summarize the Fisher matrix formalism taking into account the cross correlation between CMB and LSS, and we describe the setup for the CMB and LSS observables.

A. Fisher matrix formalism

Under the assumptions that the observables follow the Gaussian statistics, we can obtain the information on a set of parameters \mathbf{p} from the Fisher matrix written as [52]

$$F_{\ell,ij} = f_{\text{sky}} \sum_{\ell_{\min}}^{\ell_{\max}} \frac{(2\ell+1)}{2} \text{Tr} [\mathbf{C}_{\ell,i} \mathbf{C}_{\ell}^{-1} \mathbf{C}_{\ell,j} \mathbf{C}_{\ell}^{-1}], \quad (31)$$

where f_{sky} is the sky coverage of the experiment, \mathbf{C}_{ℓ} is the signal plus noise covariance matrix, and $\mathbf{C}_{\ell,i}$ is the derivative of \mathbf{C} with respect to the parameter p_i .

For CMB experiments, we consider two cases: that one is the constraint from Planck and the other is from Planck with ACTPol. It is well known that combining the results of the satellite CMB experiment with the ground based one can improve the constraints, e.g., combining WMAP with ACT[53], ACBAR[54] or so on. For these two cases, we define the total Fisher matrix as below, respectively, under the assumption for the size of survey area as $f_{\text{sky}}^{\text{ACTPol}} < f_{\text{sky}}^{\text{LSS}} < f_{\text{sky}}^{\text{Planck}}$. Here $f_{\text{sky}}^{\text{ACTPol}}$, $f_{\text{sky}}^{\text{LSS}}$ and $f_{\text{sky}}^{\text{Planck}}$ are the sky coverage of the ACTPol, the LSS and the Planck surveys, respectively, and we define the overlap region between CMB experiments and LSS surveys as $f_{\text{sky}}^{\text{Cross}}$.

• LSS + Planck:

$$F_{\ell,ij} = f_{\text{sky}}^{\text{Cross}} \sum_{\ell_{\min}=2}^{\ell_{\max}^{\text{LSS}}} \mathcal{F}_{\ell,ij}^{\text{Cross}} + f_{\text{sky}}^{\text{Planck}} \sum_{\ell_{\max}^{\text{LSS}}+1}^{\ell_{\max}^{\text{CMB}}} \mathcal{F}_{\ell,ij}^{\text{CMB}} + (f_{\text{sky}}^{\text{Planck}} - f_{\text{sky}}^{\text{Cross}}) \sum_{\ell_{\min}=2}^{\ell_{\max}^{\text{LSS}}} \mathcal{F}_{\ell,ij}^{\text{CMB}}, \quad (32)$$

	CMB	LSS	Cross: [CMB×LSS]
C_{ℓ}^{XY}	$TT, EE, \psi\psi, TE, T\psi$	$gg, \gamma\gamma, g\gamma$	$Tg, T\gamma, \psi g, \psi\gamma$
ℓ_{\max}	3000 (8000)	800	800
f_{sky}	0.65 (0.05)	0.05	0.05

TABLE IV: Survey parameters for our analysis. We assume Planck (ACTPol) for CMB experiments or their combination. For the LSS survey, we assume the HSC survey and the survey area of HSC fully overlaps with Planck or ACTPol experiments.

• LSS + Planck + ACTPol:

$$F_{\ell,ij} = f_{\text{sky}}^{\text{Cross}} \sum_{\ell_{\min}=2}^{\ell_{\max}^{\text{LSS}}} \mathcal{F}_{\ell,ij}^{\text{Cross}} \Big|_{\text{ACTPol}} + f_{\text{sky}}^{\text{ACTPol}} \sum_{\ell_{\max}^{\text{LSS}}+1}^{\ell_{\max}^{\text{CMB}}} \mathcal{F}_{\ell,ij}^{\text{CMB}} \Big|_{\text{ACTPol}} + (f_{\text{sky}}^{\text{LSS}} - f_{\text{sky}}^{\text{Cross}}) \sum_{\ell_{\min}=2}^{\ell_{\max}^{\text{LSS}}} \mathcal{F}_{\ell,ij}^{\text{Cross}} \Big|_{\text{Planck}} + (f_{\text{sky}}^{\text{Planck}} - f_{\text{sky}}^{\text{LSS}}) \sum_{\ell_{\min}=2}^{\ell_{\max}^{\text{LSS}}} \mathcal{F}_{\ell,ij}^{\text{CMB}} \Big|_{\text{Planck}} + (f_{\text{sky}}^{\text{Planck}} - f_{\text{sky}}^{\text{ACTPol}}) \sum_{\ell_{\max}^{\text{LSS}}+1}^{\ell_{\max}^{\text{CMB}}} \mathcal{F}_{\ell,ij}^{\text{CMB}} \Big|_{\text{Planck}}, \quad (33)$$

where

$$\mathcal{F}_{\ell,ij}^{\text{Cross}} = \frac{(2\ell+1)}{2} \text{Tr} [\mathbf{C}_{\ell,i}^{\text{Cross}} (\mathbf{C}_{\ell}^{\text{Cross}})^{-1} \mathbf{C}_{\ell,j}^{\text{Cross}} (\mathbf{C}_{\ell}^{\text{Cross}})^{-1}], \quad (34)$$

$$\mathcal{F}_{\ell,ij}^{\text{CMB}} = \frac{(2\ell+1)}{2} \text{Tr} [\mathbf{C}_{\ell,i}^{\text{CMB}} (\mathbf{C}_{\ell}^{\text{CMB}})^{-1} \mathbf{C}_{\ell,j}^{\text{CMB}} (\mathbf{C}_{\ell}^{\text{CMB}})^{-1}], \quad (35)$$

and different superscripts for ℓ_{\max} and f_{sky} represent different observations or CMB experiments, e.g., ℓ_{\max}^{CMB} and ℓ_{\max}^{LSS} are the maximum multipole we can take for the CMB experiment and the LSS survey, respectively. Here ℓ_{\min} is the minimum multipole we can take and we use $\ell_{\min} = 2$ in all cases. We summarize these values in Table IV.

The covariance matrix \mathbf{C}_{ℓ} and each of its matrix elements is defined as

$$[\mathbf{C}_{\ell}^{\text{Cross,CMB}}]_{\text{XY}} = C_{\ell}^{\text{XY}} + N_{\ell}^{\text{XY}} \delta_{\text{XY}}, \quad (36)$$

$$\text{where } X, Y = \begin{cases} T, E, \psi, g_i, \gamma_i & (\text{for Cross}) \\ T, E, \psi & (\text{for CMB}) \end{cases},$$

C_{ℓ}^{XY} is the angular power spectrum and N_{ℓ}^{XY} is the noise spectrum for each auto or cross correlation. We defined

N_ℓ^{TT} and N_ℓ^{EE} as N_ℓ^T and N_ℓ^P in Eq. (8), $N_\ell^{g_i g_j}$ and $N_\ell^{\gamma_i \gamma_j}$ in Eqs. (16) and (21), respectively, and $N_\ell^{\psi\psi}$ is the noise spectrum of CMB lensing potential we estimate following the technique developed in [44]. Then we assume that there is no correlation of noises between the different observables and different redshift bins. Moreover, we assume that E -mode polarization (E) has correlation only with temperature anisotropies (T) because E -mode polarization can be generated through the Thomson scattering dominantly on the last scattering surface, $C_\ell^{E\psi} = C_\ell^{Eg_i} = C_\ell^{E\gamma_i} = 0$.

Incidentally the assumption that $C_\ell^{E\psi} = 0$ is not strictly correct [55] because the large-scale polarization E -mode generated by scattering at reionization correlates with sources of CMB lensing potential over long distance. Moreover, if the galaxies are at high-redshift, the assumption that $C_\ell^{Eg_i} = 0$ is also not correct [56]. However the influence of these assumptions for our results, especially constraints on the primordial non-Gaussianity, can be small because sample galaxies in our analysis are at low redshift.

Here we explain the detail of our Fisher matrices given in Eqs. (32) and (33). In Eq. (32) the first term is responsible for the cross correlation between LSS and CMB, the second one is for CMB observables at the higher multipoles than the LSS survey can probe, and the last one is for CMB observables in the remaining survey area of CMB which does not overlap with the LSS survey. In Eq. (33) the first term is responsible for the cross correlation between LSS and CMB with ACTPol, the second one is for CMB observables with ACTPol at the higher multipoles than the LSS survey can probe, the third one is for the cross correlation between LSS and CMB with Planck in the overlapping region which does not overlap with ACTPol, the fourth one is for CMB observables with Planck in the region which does not overlap with the LSS survey, and the last one is for CMB observables with Planck at the higher multipoles than the LSS survey can probe in the region which does not overlap with ACTPol.

In our analysis, the total number of non-zero angular power spectra is 81 for the full cross correlation case ($T, E, \psi, g_i, \gamma_i$), while it is 5 for the only CMB case (T, E, ψ).

B. Setup

Given the measurement design of the surveys, we can estimate the errors in determining the cosmological parameters using the Fisher matrix formalism. The formalism tells us how well the given surveys can measure the cosmological parameters around fiducial cosmological model. Therefore, the parameter forecasts by Fisher matrix formalism depend on the choice of the fiducial model and the number of free parameters.

As for our fiducial cosmological model, we assume a

flat Λ CDM model and we include the following 9 cosmological parameters, which is based on the WMAP seven-year results [57]. The density parameters of cold dark matter, baryon and dark energy are $\Omega_c h^2$, $\Omega_b h^2$ and Ω_Λ , respectively; dark energy equation of state parameter is w ; the optical depth at reionization is τ ; and the primordial power spectrum parameters are the spectrum tilt n_S and the amplitude of the primordial power spectrum $\Delta_{\mathcal{R}}^2$ which is normalized at $k_0 = 0.002 \text{ Mpc}^{-1}$. We also include the primordial non-Gaussianity of local type modeled by the non-linear parameter f_{NL} . For specifying the galaxy bias, we include the minimum mass of halo hosting the galaxies, for which we can observe $M_{\text{obs}}[h^{-1}M_\odot]$ as a free parameter. The fiducial values are

$$\{100\Omega_b h^2, \Omega_c h^2, \Omega_\Lambda, \tau, n^S, \Delta_{\mathcal{R}}^2, w, f_{\text{NL}}, \log M_{\text{obs}}\} \\ = \{0.20, 0.1109, 0.72, 0.086, 0.96, 2.4 \times 10^{-9}, -1, 0, 11.7\}.$$

Throughout this paper we assume a spatially flat Universe, and the Hubble parameter is adjusted to keep our Universe flat when we vary Ω_Λ .

To calculate the angular power spectra C_ℓ including non-linear effects on the angular power spectrum of the galaxy distribution, cosmic shear and lensing potential, we use the CAMB code [58] and the HALOFIT code [59]. We, however, want to remove the burden of the uncertainty of the non-linear calculation as much as possible, so our estimation preferably is based on the information from large-scale for LSS where the linear prediction is reliable.

In our estimation, we include the information from temperature anisotropies (T), E -mode polarization (E) and reconstructed lensing potential (ψ) for CMB. The range of multipoles are $2 \leq \ell \leq 3000$ and the survey area is taken as $f_{\text{sky}} = 0.65$ for Planck and $f_{\text{sky}} = 0.05$ for ACTPol, respectively. On the other hand, for the galaxy survey (g) and galaxy weak lensing survey (γ), the ranges of multipole are $2 \leq \ell \leq 800$ and the survey areas are $f_{\text{sky}} = 0.05$ for both of them with HSC. Furthermore we take into account all the cross correlation we can consider and we assume the optimal condition that there is no correlation between different patches, so that the area having a correlation between CMB and LSS corresponds to the overlapped survey area. We summarize the values we use in the following calculation in TABLE IV.

VI. RESULT

A. Signal-to-Noise ratio

To see the errors in the cross correlation power spectra more quantitatively, we estimate the signal-to-noise ratio (S/N) for each ℓ -bin and the cumulative (S/N). We define the $(S/N)^2$ for a cross correlation between X and Y , following [60], as

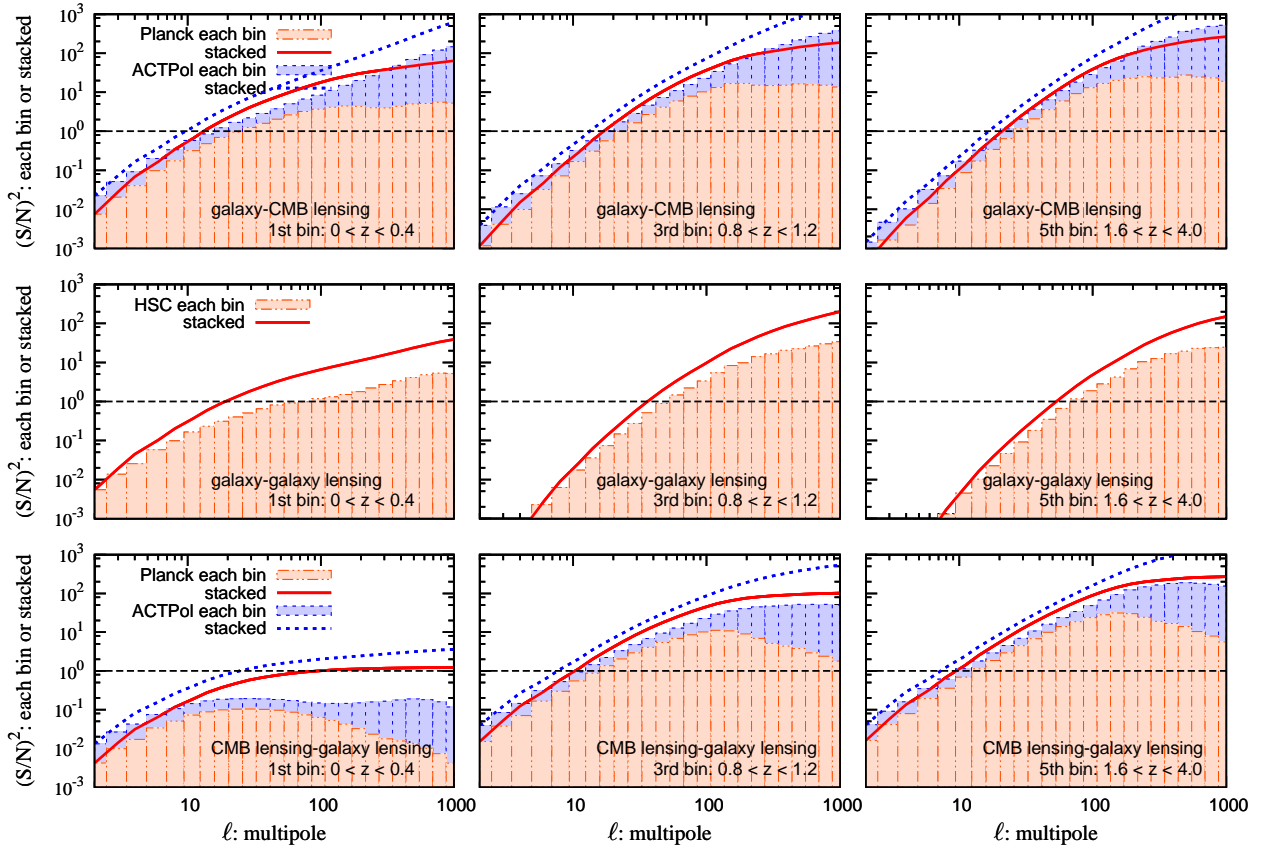


FIG. 3: Signal-to-Noise ratio for some angular power spectra. We show the S/N for each bin (box) and stacked S/N (line), respectively. Top panels are for galaxy-CMB lensing ($g_i\psi_j$) angular power spectra, Center ones are for galaxy-galaxy lensing ($g_i\gamma_j$), and Bottom ones are for CMB lensing-galaxy lensing ($\psi_i\gamma_j$) based on the fiducial model of Fig. 2.

- S/N for each ℓ -bin:

$$\left(\frac{S}{N}\right)^2(\ell) \equiv f_{\text{sky}} \sum_{\ell_{\min}^{(i)}}^{\ell_{\max}^{(i)}} (2\ell + 1) \times \frac{(C_{\ell}^{\text{XY}})^2}{(C_{\ell}^{\text{XX}} + N_{\ell}^{\text{XX}})(C_{\ell}^{\text{YY}} + N_{\ell}^{\text{YY}}) + (C_{\ell}^{\text{XY}})^2}, \quad (37)$$

- stacked S/N :

$$\left(\frac{S}{N}\right)^2(\leq \ell_{\max}) \equiv f_{\text{sky}} \sum_{\ell=2}^{\ell_{\max}} (2\ell + 1) \times \frac{(C_{\ell}^{\text{XY}})^2}{(C_{\ell}^{\text{XX}} + N_{\ell}^{\text{XX}})(C_{\ell}^{\text{YY}} + N_{\ell}^{\text{YY}}) + (C_{\ell}^{\text{XY}})^2}, \quad (38)$$

where $\ell_{\max}^{(i)}$ and $\ell_{\min}^{(i)}$ are the maximum and minimum multipoles of the i -th multipole bin, respectively, C_{ℓ}^{XY} and N_{ℓ}^{XX} , N_{ℓ}^{YY} are the fiducial and noise spec-

tra, respectively. The index X, Y represents $\{X, Y\} \in \{T, E, \psi, g, \gamma\}$.

Figure 3 shows an example of $(S/N)^2$ for each ℓ given by Eq. (37) and cumulative $(S/N)^2$ by Eq. (38), for the galaxy-galaxy lensing ($g\gamma$), galaxy-CMB lensing ($g\psi$) and CMB lensing-galaxy lensing ($\psi\gamma$) cross correlations. For the galaxy-CMB lensing and CMB lensing-galaxy lensing with HSC-Planck experiments, the amplitude of $(S/N)^2$ decreases at high- ℓ bins and the stacked $(S/N)^2$ saturates due to the noise of CMB lensing at small scales. On the other hand, we can expect the larger $(S/N)^2$ at high- ℓ bins for the case with HSC-ACTPol. The amplitude of $(S/N)^2$ at low- ℓ bins where the signature of the primordial non-Gaussianity shines out is very low in all the cases. However, comparing galaxy-CMB lensing with galaxy-galaxy lensing signals, the amplitude of the former is larger than the latter in high-redshift bins and the difference becomes even greater for the with HSC-ACTPol.

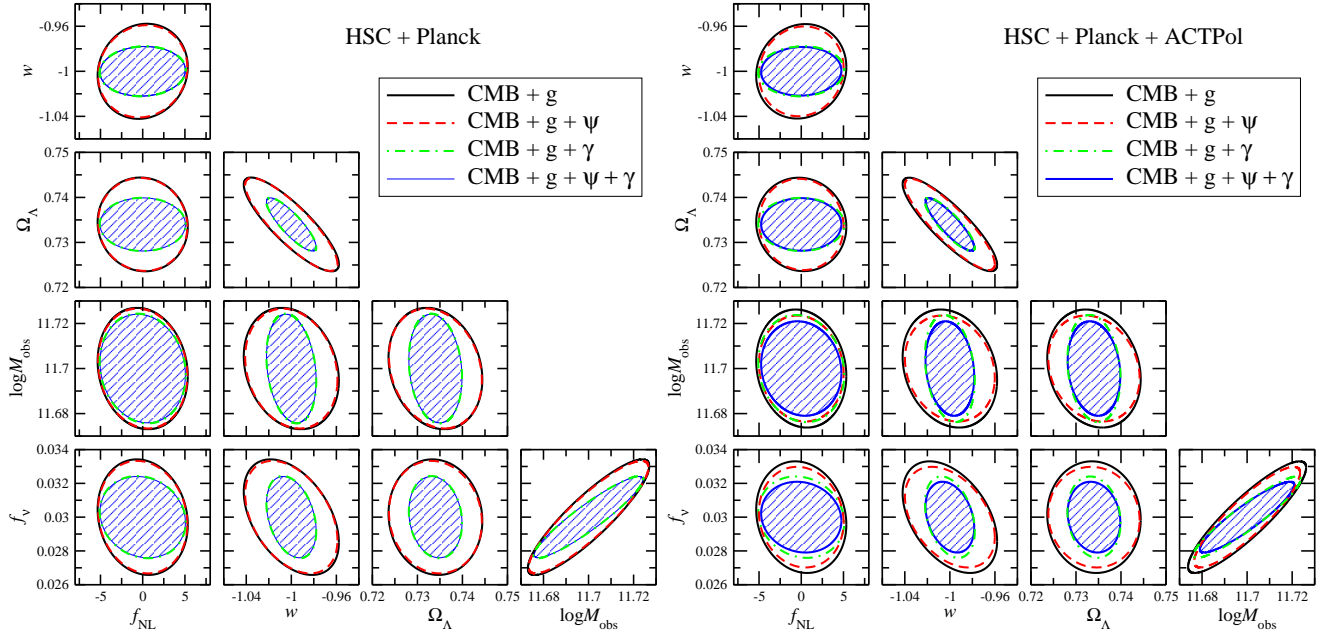


FIG. 4: Projected $1\sigma(68\%)$ confidence constraints in some parameter spaces for the $f_\nu \neq 0$ model. We show contours from CMB and galaxy distribution (black thick); from CMB, galaxy distribution and CMB lensing (red dashed); from CMB, galaxy distribution and galaxy lensing (green dot-dashed); and from all the observables (blue thin). All auto and cross correlations between these observables are taken into account for the constraints. Here we assume the HSC survey and Planck experiment (Left) or HSC and combination of Planck and ACTPol (Right).

	$100\Omega_b h^2$	$\Omega_c h^2$	Ω_Λ	τ	f_ν	n^S	$\Delta_{\mathcal{R}}^2 \times 10^{-9}$	w	f_{NL}	$\log M_{obs}$
galaxy clustering only (HSC): C_ℓ^{gg}	0.94	0.026	0.011	0.11	0.029	0.13	0.49	0.053	5.9	0.60
HSC + Planck										
CMB only	0.015	0.0013	0.19	0.0050	0.020	0.0047	0.042	0.69	—	—
CMB + C_ℓ^{gg}	0.011	0.00055	0.010	0.0044	0.0034	0.0027	0.029	0.042	5.4	0.027

CMB + $C_\ell^{gg} + C_\ell^{Tg}$	0.011	0.00055	0.010	0.0044	0.0034	0.0027	0.029	0.042	5.3	0.027
+ $C_\ell^{\psi\psi} + C_\ell^{\psi g} + C_\ell^{T\psi}$	0.011	0.00053	0.010	0.0043	0.0033	0.0027	0.028	0.041	5.3	0.027
+ $C_\ell^{\gamma\gamma} + C_\ell^{\gamma g} + C_\ell^{T\gamma}$	0.011	0.00031	0.0059	0.0044	0.0024	0.0024	0.027	0.022	5.1	0.024
+ $C_\ell^{\psi\psi} + C_\ell^{\gamma\gamma} + C_\ell^{\psi g} + C_\ell^{\gamma g}$										
+ $C_\ell^{T\psi} + C_\ell^{T\gamma} + C_\ell^{\psi\gamma}$	0.011	0.00031	0.0059	0.0043	0.0024	0.0023	0.026	0.022	5.1	0.024
HSC + Planck + ACTPol										
CMB only	0.0076	0.0010	0.18	0.0046	0.018	0.0038	0.036	0.66	—	—
CMB + C_ℓ^{gg}	0.0076	0.00052	0.010	0.0041	0.0033	0.0025	0.028	0.042	5.4	0.026

CMB + $C_\ell^{gg} + C_\ell^{Tg}$	0.0076	0.00052	0.010	0.0041	0.0033	0.0025	0.028	0.042	5.3	0.026
+ $C_\ell^{\psi\psi} + C_\ell^{\psi g} + C_\ell^{T\psi}$	0.0076	0.00050	0.010	0.0039	0.0030	0.0024	0.026	0.040	5.0	0.024
+ $C_\ell^{\gamma\gamma} + C_\ell^{\gamma g} + C_\ell^{T\gamma}$	0.0074	0.00030	0.0059	0.0041	0.0024	0.0022	0.025	0.022	5.1	0.024
+ $C_\ell^{\psi\psi} + C_\ell^{\gamma\gamma} + C_\ell^{\psi g} + C_\ell^{\gamma g}$										
+ $C_\ell^{T\psi} + C_\ell^{T\gamma} + C_\ell^{\psi\gamma}$	0.0073	0.00029	0.0058	0.0039	0.0021	0.0022	0.024	0.022	4.8	0.021

TABLE V: Expected marginalized error (1σ) and these forecasts correspond to the results of Fig. 4.

B. Constraints on the primordial non-Gaussianity

We estimate the errors in the determination of cosmological parameters for the HSC-like survey using the Fisher matrix formalism, and show the main results,

namely, the 1σ confidence limit constraints in Fig. 4 and Table V, in which we consider 10 cosmological parameters: the fraction of the massive neutrino density parameter to the matter density parameter $f_\nu (= 0.03) = \Omega_\nu/\Omega_m$ in addition to the nine cosmological parameters defined

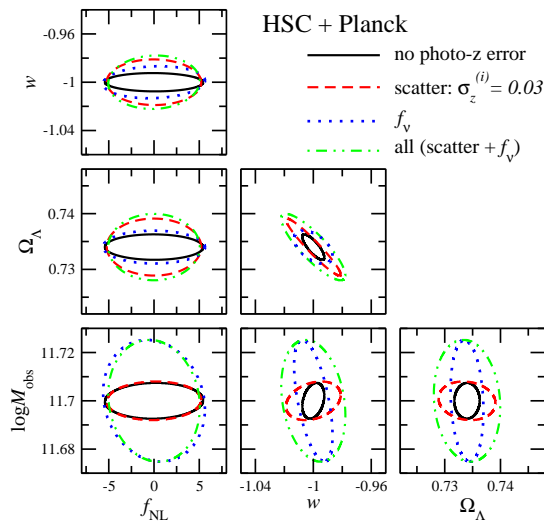


FIG. 5: Projected $1\sigma(68\%)$ confidence constraints in some parameter spaces from Planck and HSC experiments including auto and cross correlations between CMB, CMB lensing, galaxy distribution and galaxy lensing. We show the contours with or without the photometric redshift scatter for the Λ CDM model, the contours without the photometric redshift scatter for the $f_\nu \neq 0$ model and the contour with the photometric redshift scatter for the $f_\nu = 0$ model.

in Sec. VB.

The simplest case, which is from only galaxy clustering, puts the constraint on f_{NL} as $\Delta f_{\text{NL}} \sim 5.9$, and the constraint can be improved to $\Delta f_{\text{NL}} \sim 5.4$ by combining the CMB-only result though CMB has no information about primordial non-Gaussianity on the level of the 2-point function without cross correlations with galaxy clustering. This is because the information from CMB helps to determine the galaxy bias by breaking degeneracies with other cosmological parameters, and then the degeneracy between f_{NL} and M_{obs} can be broken effectively. Hence the constraint on M_{obs} is also improved dramatically after combining CMB information, which can be seen in Table V, and these tendencies have been seen in our previous analysis [48].

We show four cases to see the improvement by adding the different observables in Fig. 4. In the first case we use CMB and galaxy distribution (CMB + g); in the second case we add CMB lensing to the first case (CMB + g + ψ); in the third case we add shear to the first case (CMB + g + γ); and in the last case we use all the information available. We take into account all the available power spectra. The selection of auto and cross correlations in Fig. 4 and Table V corresponds to each other in each case. We obtain the constraints on f_{NL} as $\Delta f_{\text{NL}} \sim 5.1$ with Planck and HSC. Moreover, we can improve the constraint by including ACTPol as $\Delta f_{\text{NL}} \sim 4.8$, thanks to the galaxy-CMB lensing cross correlations.

VII. DISCUSSION

A. Selection of the fiducial model

We assume imaging surveys for the LSS galaxy surveys, and we have to take into account the influence of the various systematics, e.g., magnification effects due to gravitational lensing [61], photometric redshift(photo- z) errors [51] and so on (see, for example, [49, 50]). Moreover, as mentioned in the previous section, the parameter forecasts by Fisher matrix formalism depend on the choice of the fiducial model and free parameters. In Fig. 5, we summarize the effects of selecting fiducial models.

1. Photometric redshift error

For the constraint on f_{NL} , any significant difference is not found between with and without the photometric redshift scatter systematics. This is because the redshift scatter changes the overall amplitude of the galaxy distribution (g) and cosmic shear (γ) as shown in Fig. 2. On the other hand, the effect of non-Gaussianity, f_{NL} , emerges only at large angular scales, and it can be distinguishable. However, the effects of the photometric redshift error are significant for the parameters which are determined through the information about the redshift evolution such as Ω_Λ and w . Although the effect of the parameter M_{obs} is to change the bias parameter and is similar to the effect of the redshift scatter, a significant difference is not found in the figure.

2. Massive neutrino

Various experiments, such as ground based experiments of neutrino oscillation, predict the non-zero neutrino mass [62, 63]. Therefore, we need to include the mass of neutrinos for a more accurate estimation of the cosmological parameters. There are, however, some debatable subtle arguments about taking the mass of neutrinos into account in models for the mass function and the halo bias. These models have been tested by N-body simulations without massive neutrinos and are not guaranteed enough for cosmological models with massive neutrinos. The analytic formula for the scale-dependent bias presented in Eq. (4) is also for models without massive neutrinos.

For the mass function, it is found that the influence of massive neutrinos is very small [64]. Thus, we just assume that the halo mass function and halo bias models can be applied even if the massive neutrinos are included.

Comparing the results of $f_\nu = 0$ and $f_\nu \neq 0$ models in Fig. 5, a significant difference can be seen in the constraint on M_{obs} . The existence of massive neutrinos affects the large-scale structure formation through its large velocity dispersion and alter the amplitude of the matter power spectrum. This effect is similar to the effect from

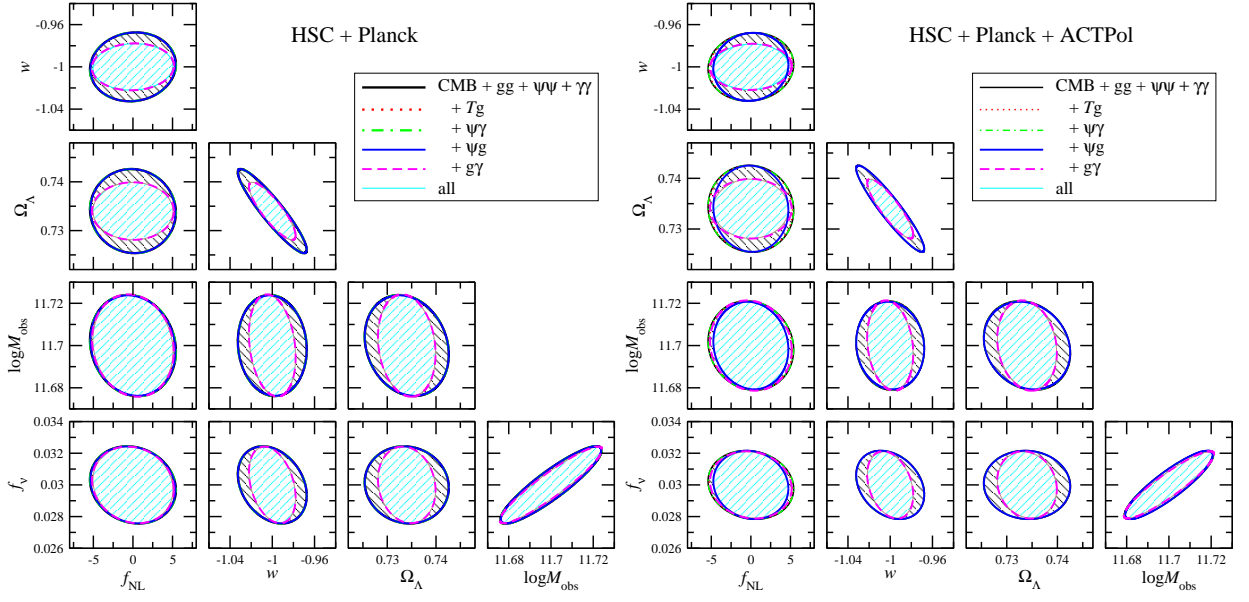


FIG. 6: Same as Fig. 4 but we highlight the contribution from the cross correlations to the constraints. The base constraints are from CMB(TT, EE, TE), galaxy distribution (gg), CMB lensing ($\psi\psi$) and galaxy lensing ($\gamma\gamma$) auto correlations (black thin line). The other contours show improvements by including cross correlation as indicated in the figure. Here we consider the HSC survey and Planck with and without ACTPol experiment (left and right panels, respectively).

	$100\Omega_b h^2$	$\Omega_c h^2$	Ω_Λ	τ	f_ν	n^S	$\Delta_{\mathcal{R}}^2 \times 10^{-9}$	w	f_{NL}	$\log M_{\text{obs}}$
HSC + Planck										
CMB + $C_\ell^{\text{gg}} + C_\ell^{\psi\psi} + C_\ell^{\gamma\gamma}$	0.011	0.00034	0.0086	0.0043	0.0024	0.0024	0.026	0.033	5.4	0.024
+ C_ℓ^{Tg}	0.011	0.00034	0.0086	0.0043	0.0024	0.0024	0.026	0.033	5.3	0.024
+ $C_\ell^{\psi\gamma}$	0.011	0.00034	0.0086	0.0043	0.0024	0.0024	0.026	0.033	5.4	0.024
+ $C_\ell^{\psi g}$	0.011	0.00034	0.0086	0.0043	0.0024	0.0024	0.026	0.033	5.4	0.024
+ $C_\ell^{g\gamma}$	0.011	0.00031	0.0059	0.0043	0.0024	0.0023	0.026	0.022	5.2	0.024
+ $C_\ell^{Tg} + C_\ell^{\psi\gamma} + C_\ell^{\psi g} + C_\ell^{g\gamma}$	0.011	0.00031	0.0059	0.0043	0.0024	0.0023	0.026	0.022	5.1	0.024
HSC + Planck + ACTPol										
CMB + $C_\ell^{\text{gg}} + C_\ell^{\psi\psi} + C_\ell^{\gamma\gamma}$	0.0074	0.00033	0.0086	0.0039	0.0022	0.0022	0.024	0.032	5.4	0.021
+ C_ℓ^{Tg}	0.0074	0.00033	0.0086	0.0039	0.0022	0.0022	0.024	0.032	5.3	0.021
+ $C_\ell^{\psi\gamma}$	0.0073	0.00032	0.0085	0.0039	0.0022	0.0022	0.024	0.032	5.4	0.021
+ $C_\ell^{\psi g}$	0.0073	0.00033	0.0085	0.0039	0.0022	0.0022	0.024	0.032	4.8	0.021
+ $C_\ell^{g\gamma}$	0.0073	0.00030	0.0059	0.0039	0.0021	0.0022	0.024	0.022	5.1	0.021
+ $C_\ell^{Tg} + C_\ell^{\psi\gamma} + C_\ell^{\psi g} + C_\ell^{g\gamma}$	0.0073	0.00029	0.0058	0.0039	0.0021	0.0022	0.024	0.022	4.8	0.021

TABLE VI: Expected marginalized errors (1σ) and these forecasts correspond to the results of Fig. 6.

M_{obs} and these two parameters are strongly degenerated with each other as shown in Fig. 4. Note that the de-grade of the constraint on M_{obs} in the case of the $f_\nu \neq 0$ model comes from the strong degeneracy between them and we have confirmed that there is little change in the constraint if we fix the value of f_ν (and do not take it as a free parameter). For the constraints on f_{NL} itself, however, the difference of the fiducial models whether $f_\nu = 0$

or not is not so significant.

In summary, focusing on the constraint of f_{NL} , the selection of the fiducial model makes little impact on the result. On the other hand, the constraints on some other parameters depend on the fiducial model, especially on the existence of neutrino mass and photometric redshift error.

B. Contribution of cross correlations

Now let us discuss the contribution from ACTPol experiment which will extract the information of CMB lens-

ing more efficiently than Planck.

	HSC + Planck					HSC + Planck + ACTPol				
	Ω_Λ	f_ν	w	f_{NL}	$\log M_{\text{obs}}$	Ω_Λ	f_ν	w	f_{NL}	$\log M_{\text{obs}}$
CMB + C_ℓ^{gg} + $C_\ell^{\psi\psi}$ + $C_\ell^{\gamma\gamma}$	0.015	0.0028	0.054	5.5	0.033	0.015	0.0023	0.053	5.4	0.029
+ C_ℓ^{Tg}	0.015	0.0028	0.053	5.4	0.033	0.014	0.0023	0.053	5.3	0.029
+ $C_\ell^{\psi\gamma}$	0.015	0.0028	0.053	5.5	0.033	0.014	0.0023	0.053	5.4	0.029
+ $C_\ell^{\psi g}$	0.015	0.0028	0.053	5.4	0.033	0.014	0.0023	0.051	4.8	0.028
+ $C_\ell^{g\gamma}$	0.0095	0.0028	0.035	5.2	0.033	0.0095	0.0023	0.034	5.2	0.029
All	0.0095	0.0028	0.034	5.1	0.033	0.0092	0.0023	0.033	4.8	0.028

TABLE VII: Expected marginalized errors (1σ) which correspond to the results of Fig. 8 with all systematics. This table should be compared with TABLE VI where the systematics are neglected.

As shown Fig. 4 and Table V, we find that almost all the constraints on each plane are determined through galaxy lensing information except for M_{obs} and f_{NL} . However, CMB lensing also gives important contributions if the ACTPol experiment is included. Focusing on the constraints on the $f_{\text{NL}}-M_{\text{obs}}$ plane, both the CMB lensing and galaxy lensing signals improve the constraints slightly by including their cross correlations, though the most of the constraints are determined by the galaxy auto correlation.

We show how the cross correlations improve the constraints in Fig. 6 and Table VI. We find that most of the constraints are mainly determined through the auto correlations on each plane but we can still gain a little benefit from the cross correlations. By including all cross correlations among CMB, galaxy distribution and galaxy lensing shear, we can expect 5.6% improvement for the constraint on f_{NL} with HSC and Planck, and 11.1% improvement with HSC, Planck and ACTPol. In particular, the impact of the cross correlation between galaxy and galaxy lensing ($g\gamma$) is significant, especially in the $w-\Omega_\Lambda$ plane. This result is consistent with that obtained by [31, 61] and $g\gamma$ will play a very important role in the constraint on dark energy parameters.

Finally, to see the impact of cross correlations for the constraint on the primordial non-Gaussianity, let us focus on the constraints on the $f_{\text{NL}}-M_{\text{obs}}$ plane in Fig. 6. We find that the cross correlation between galaxy and CMB lensing ($g\psi$) will improve the constraint on f_{NL} when the Planck and ACTPol experiments are combined. However we have little benefit from the cross correlations if we use only Planck for the CMB experiment.

C. Dependence on mass threshold M_{obs}

The parameter M_{obs} reflects the mass threshold we can observe as galaxy and relates to the galaxy bias through Eq. (13). We can interpret from Fig. 1 that the larger value of M_{obs} predicts the larger bias. We show the constraints for the different fiducial value of M_{obs} in Fig. 7. Only in this figure, we plot $\Delta \log M_{\text{obs}}$ instead of $\log M_{\text{obs}}$ for the purpose of illustrating the different fiducial models on the same planes.

The difference which comes from the different fiducial values of M_{obs} appears especially in the constraints on f_{NL} and M_{obs} , while the constraints on the other parameters are not altered so much. This is because the constraints on f_{NL} and M_{obs} come mainly from the galaxy distribution (g), while the constraints of the others come mainly from the other observables. As for the constraints on f_{NL} , the larger value of M_{obs} can lead to a tighter constraint on f_{NL} . The larger value of M_{obs} means picking out the higher mass objects. Because high mass objects exhibit a large bias, the non-Gaussian correction to the bias becomes large. Furthermore, the correction to the mass function also becomes large for high mass objects. For these reasons, the effect of the non-Gaussianity through the effective bias b_{eff} becomes clearer when we choose the larger values of M_{obs} for the fiducial model. Thus we can constrain f_{NL} more tightly for larger the value of M_{obs} .

D. Effects of photometric redshift systematics

Here, we investigate effects of photometric redshift systematics on the parameter constraints following examples in [50].

In our analysis, we assume the fiducial redshift scatter and bias as Eqs. (29) and (30), respectively. To characterize the uncertainty in the scatter and bias, we parameterize $\sigma_z^{(i)}$ and $z_{\text{bias}}^{(i)}$ ($i = \{1, 2, 3, 4, 5\}$) in 5 bins, include these 10 parameters in the Fisher matrix, apply a prior of 0.01 on each, and finally marginalize over these parameters. We show the effects of the photometric redshift systematics on constraints on some parameters in Fig. 8 and Table VII.

In Fig. 8, we show the total effects of the scatter and bias on the parameter determination, as well as the individual effects. The scatter gives a stronger impact than the bias, and including both of the two systematics dramatically enlarges the constraint contours, except for f_ν and f_{NL} . Perhaps, for f_ν , the constraint comes mainly from CMB and CMB lensing, so the effects of systematics in the LSS observables do not contribute to the constraint. For the constraint on f_{NL} , the effects of systematics have little degeneracies with the effect of f_{NL}

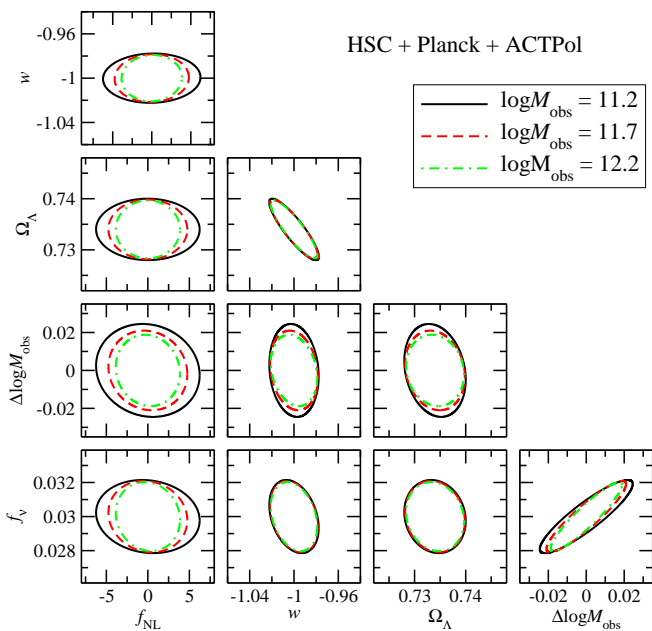


FIG. 7: Projected $1\sigma(68\%)$ confidence constraints in some parameter spaces for three fiducial values of the mass threshold $M_{\text{obs}}[h^{-1}M_{\odot}] = 10^{11.2}, 10^{11.7}, 10^{12.2}$. We show the contours expected from combining HSC, Planck and ACTPol, and these results include all the information from the auto and cross correlations. Only in this figure, we plot the deviation from the fiducial values $\Delta \log M_{\text{obs}}$ instead of $\log M_{\text{obs}}$ for the purpose of illustrating the different fiducial models on the same planes.

because we can distinguish these effects through the observation of the power spectra at large-scale region (low- ℓ region).

In Table VII, we show 1σ errors for some parameters in the case with HSC and Planck experiments, with or without ACTPol, sorted by the cross correlation spectrum used in the analysis. The relative amount of contributions from each cross correlation to the constraints is similar to the case without systematics. However, we enjoy the benefits of including the extra cross correlations more in the case with systematics than without. For example, information from the cross correlation brings 38.7% and 37.7% improvements of the constraints on Ω_{Λ} and w in the case with systematics, respectively, while bringing 32.6% and 31.3% improvements in the case without systematics.

E. Comparison with other various future surveys

Focusing on the constraints on the primordial non-Gaussianity from the galaxy power spectrum or two-point correlation function using the scale-dependent bias, the result significantly depends on the survey strategies. The signature of the primordial non-Gaussianity grows with redshift and appears prominently on the large-scale,

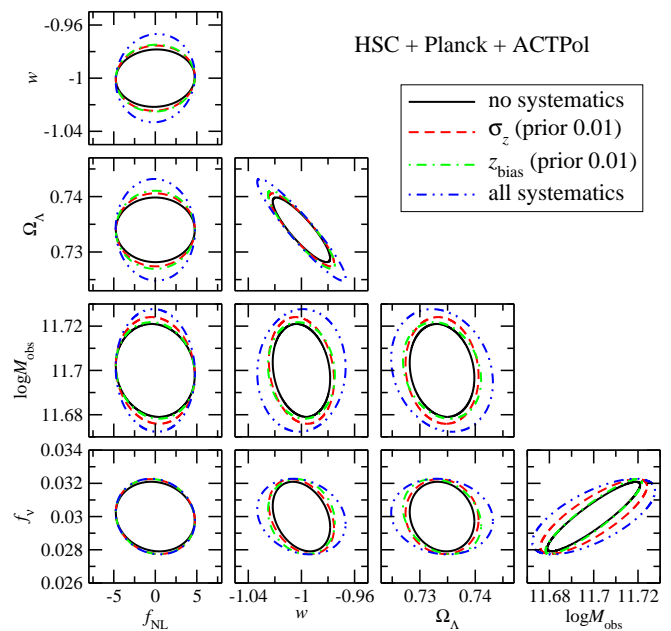


FIG. 8: Projected $1\sigma(68\%)$ confidence constraints in some parameter spaces without photometric redshift systematics, including the effects of scatter and bias individually, and including the both of the effects simultaneously. The contours are obtained from HSC, Planck and ACTPol, and the results include the information from all auto and cross correlations.

so surveys observing high-redshift and wide area are predictably effective for this purpose. Here, we show the constraints expected from other survey projects besides HSC, such as DES [27] and LSST [28] in Fig. 9.

Comparing the HSC survey with DES, the DES survey is more suitable for the constraints on the parameters related to dark energy, such as Ω_{Λ} and w , than HSC. For the constraint on the primordial non-Gaussianity, however, HSC is more suitable than DES. This is because HSC will observe galaxies in higher redshift than DES and it allows us to follow the redshift evolution of the scale-dependent bias due to the primordial non-Gaussianity, even though the survey area of DES is larger than HSC. On the other hand, the constraints from LSST are tremendous for most of the parameter determinations.

VIII. SUMMARY

In this work, we estimated errors in the determination of cosmological parameters for some future surveys with the Fisher matrix method, newly including galaxy-galaxy lensing ($g\gamma$) and CMB lensing-galaxy lensing ($\psi\gamma$) cross correlations. In general, the extra information from cross correlations allows us to estimate the cosmological parameters more precisely.

As for the constraint on the $f_{\text{NL}}\text{-}\log M_{\text{obs}}$ plane, galaxy-galaxy lensing ($g\gamma$) cross correlation improves the

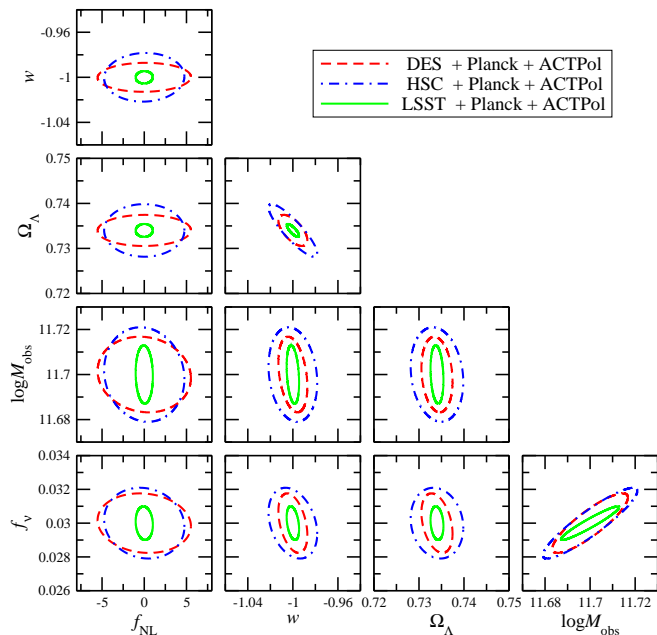


FIG. 9: Projected $1\sigma(68\%)$ confidence constraints in some parameter spaces for $f_\nu \neq 0$ model with the photometric redshift scatter. The contours are for DES (red dashed), HSC (blue dot-dashed) or LSST (green), with Planck and ACTPol combined. The results include all the information from auto and cross correlations.

constraint greatly. On the other hand, galaxy-CMB lensing ($g\psi$) cross correlation can also improve the constraint if the ACTPol experiment is included.

Although galaxy-galaxy lensing ($g\gamma$) cross correlation has a great contribution for improving the constraint on f_{NL} , we have to pay attention to the systematics of galaxy lensing observation. The photo- z error diffuses the observed galaxy distribution of each redshift bin, and changes the overall amplitude of the power spectrum. This behavior is similar to the change of the parameter $\log M_{\text{obs}}$. On the other hand, positive (negative) f_{NL} enhances (decreases) the amplitude only on large-scales. Therefore comparing these two parameters, the constraint on $\log M_{\text{obs}}$ is more affected by photo- z error than that of f_{NL} .

Here, we accounted only for the photo- z error for systematics, but it is known that there are other systematics for the galaxy lensing observables. One of them is a complication in the measurement of the shear due to the incomplete removal of the effects of the point spread function (PSF) [65]. So the contribution of galaxy-galaxy lensing ($g\gamma$) cross correlation to the constraint on f_{NL} may be diminished if we consider a more realistic condition including other systematics for galaxy lensing observables. In such a case, the impact of galaxy-CMB lensing ($g\psi$) cross correlation probably shines out more.

In general, the choice of the fiducial cosmological model

affects the parameter forecasts. In this paper, we considered the differences of the fiducial model in the neutrino mass and the photometric redshift scatter. As far as the constraint on f_{NL} is concerned, we found that the selection of the fiducial model makes an impact on the result.

It should be emphasized that combining the satellite CMB experiment (Planck) with the ground based one (ACTPol) can greatly improve the constraints on the cosmological parameters. This is because the information of CMB lensing can be extracted more efficiently by combining Planck with ACTPol than by Planck only. For the constraint on f_{NL} , the marginalized error can be improved from $\Delta f_{\text{NL}} \sim 5.1$ to 4.8 by combining ACTPol with Planck, because in this case galaxy-CMB lensing cross correlation ($g\psi$) starts to play an important role in the improvement of the statistical error of f_{NL} .

As for the strategy of the survey, we found that HSC is preferable to DES for the constraint on f_{NL} because the former can probe higher redshift. We expect $\Delta f_{\text{NL}} \sim 5.5$ with the DES survey while $\Delta f_{\text{NL}} \sim 4.8$ with HSC. However, we never forget the importance of wide field surveys to see the signature of the primordial non-Gaussianity appearing on large-scale.

As for the benefits from the cross correlations, we found that the cross correlation between CMB lensing and galaxy distribution improves the constraints on f_{NL} from 5.4 to 4.8 ($\Delta 11.1\%$), and from 1.1 to 1.0 ($\Delta 8.3\%$) in the case with LSST. The relative improvement of f_{NL} by including cross correlations is less distinct in LSST, but the cross correlation will be still significant in the future surveys.

Acknowledgments

We thank O. Doré, S. Dodelson, A. Lewis, T. Namikawa, and S. Yokoyama for useful discussion and comments. We acknowledge support from JSPS (Japan Society for Promotion of Science) Grant-in-Aid for Scientific Research under Grant No. 22012004 (KI); Grant-in-Aid for Nagoya University Global COE Program “Quest for Fundamental Principles in the Universe: from Particles to the Solar System and the Cosmos”, from the Ministry of Education, Cluster, Sports, Science, and Technology (MEXT); Kobayashi-Maskawa Institute for the Origin of Particles and the Universe; Nagoya University for providing computing resources useful in conducting the research reported in this paper, Grant-in-Aid for Scientific Research (C), under Grant No. 21540263, 2009 (TM); and Grant-in-Aid for Scientific Research on Priority Areas No. 467 “Probing the Dark Energy through an Extremely Wide and Deep Survey with Subaru Telescope”. This work is supported in part by JSPS Core-to-Core Program “International Research Network for Dark Energy”.

-
- [1] V. F. Mukhanov and G. V. Chibisov, *Soviet Journal of Experimental and Theoretical Physics Letters* **33**, 532 (1981).
- [2] T. J. Allen, B. Grinstein, and M. B. Wise, *Physics Letters B* **197**, 66 (1987).
- [3] A. Gangui, F. Lucchin, S. Matarrese, and S. Mollerach, *Astrophys. J.* **430**, 447 (1994), arXiv:astro-ph/9312033.
- [4] J. Maldacena, *Journal of High Energy Physics* **5**, 13 (2003), arXiv:astro-ph/0210603.
- [5] V. Acquaviva, N. Bartolo, S. Matarrese, and A. Riotto, *Nuclear Physics B* **667**, 119 (2003), arXiv:astro-ph/0209156.
- [6] E. Komatsu, A. Kogut, M. R. Nolta, C. L. Bennett, M. Halpern, G. Hinshaw, N. Jarosik, M. Limon, S. S. Meyer, L. Page, et al., *Astrophys. J Supp.* **148**, 119 (2003), arXiv:astro-ph/0302223.
- [7] D. N. Spergel, R. Bean, O. Doré, M. R. Nolta, C. L. Bennett, J. Dunkley, G. Hinshaw, N. Jarosik, E. Komatsu, L. Page, et al., *Astrophys. J Supp.* **170**, 377 (2007), arXiv:astro-ph/0603449.
- [8] P. Creminelli, L. Senatore, M. Zaldarriaga, and M. Tegmark, *JCAP* **3**, 5 (2007), arXiv:astro-ph/0610600.
- [9] E. Komatsu, J. Dunkley, M. R. Nolta, C. L. Bennett, B. Gold, G. Hinshaw, N. Jarosik, D. Larson, M. Limon, L. Page, et al., *Astrophys. J Supp.* **180**, 330 (2009), 0803.0547.
- [10] K. M. Smith, L. Senatore, and M. Zaldarriaga, *JCAP* **9**, 6 (2009), 0901.2572.
- [11] E. Komatsu, K. M. Smith, J. Dunkley, C. L. Bennett, B. Gold, G. Hinshaw, N. Jarosik, D. Larson, M. R. Nolta, L. Page, et al., *Astrophys. J Supp.* **192**, 18 (2011), 1001.4538.
- [12] M. Lo Verde, A. Miller, S. Shandera, and L. Verde, *JCAP* **4**, 14 (2008), 0711.4126.
- [13] S. Matarrese, L. Verde, and R. Jimenez, *Astrophys. J.* **541**, 10 (2000), arXiv:astro-ph/0001366.
- [14] L. Verde, R. Jimenez, M. Kamionkowski, and S. Matarrese, *Mon. Not. R. Astron. Soc.* **325**, 412 (2001), arXiv:astro-ph/0011180.
- [15] G. D'Amico, M. Musso, J. Noreña, and A. Paranjape, *JCAP* **2**, 1 (2011), 1005.1203.
- [16] M. Grossi, L. Verde, C. Carbone, K. Dolag, E. Branchini, F. Iannuzzi, S. Matarrese, and L. Moscardini, *Mon. Not. R. Astron. Soc.* **398**, 321 (2009), 0902.2013.
- [17] S. Yokoyama, N. Sugiyama, S. Zaroubi, and J. Silk, *Mon. Not. R. Astron. Soc. pp.* 1297–+ (2011), 1103.2586.
- [18] A. Slosar, C. Hirata, U. Seljak, S. Ho, and N. Padmanabhan, *JCAP* **8**, 31 (2008), 0805.3580.
- [19] N. Dalal, O. Doré, D. Huterer, and A. Shirokov, *Phys. Rev. D* **77**, 123514 (2008), 0710.4560.
- [20] N. Afshordi and A. J. Tolley, *Phys. Rev. D* **78**, 123507 (2008), 0806.1046.
- [21] S. Matarrese and L. Verde, *Astrophys. J Lett.* **677**, L77 (2008), 0801.4826.
- [22] S. Yokoyama, ArXiv e-prints (2011), 1108.5569.
- [23] J.-O. Gong and S. Yokoyama, *Mon. Not. R. Astron. Soc. pp.* L313+ (2011), 1106.4404.
- [24] V. Desjacques, U. Seljak, and I. T. Iliev, *Mon. Not. R. Astron. Soc.* **396**, 85 (2009), 0811.2748.
- [25] J.-Q. Xia, C. Baccigalupi, S. Matarrese, L. Verde, and M. Viel, ArXiv e-prints (2011), 1104.5015.
- [26] S. Miyazaki, Y. Komiyama, H. Nakaya, Y. Doi, H. Furusawa, P. Gillingham, Y. Kamata, K. Takeshi, and K. Narai, in *Society of Photo-Optical Instrumentation Engineers (SPIE) Conference Series* (2006), vol. 6269 of *Society of Photo-Optical Instrumentation Engineers (SPIE) Conference Series*.
- [27] The Dark Energy Survey Collaboration, ArXiv Astrophysics e-prints (2005), arXiv:astro-ph/0510346.
- [28] LSST Science Collaborations, P. A. Abell, J. Allison, S. F. Anderson, J. R. Andrew, J. R. P. Angel, L. Armus, D. Arnett, S. J. Asztalos, T. S. Axelrod, et al., ArXiv e-prints (2009), 0912.0201.
- [29] C. Carbone, L. Verde, and S. Matarrese, *Astrophys. J Lett.* **684**, L1 (2008), 0806.1950.
- [30] C. Carbone, O. Mena, and L. Verde, *JCAP* **7**, 20 (2010), 1003.0456.
- [31] M. Oguri and M. Takada, *Phys. Rev. D* **83**, 023008 (2011), 1010.0744.
- [32] C. Cunha, D. Huterer, and O. Doré, *Phys. Rev. D* **82**, 023004 (2010), 1003.2416.
- [33] R. K. Sachs and A. M. Wolfe, *Astrophys. J.* **147**, 73 (1967).
- [34] D. Jeong, E. Komatsu, and B. Jain, *Phys. Rev. D* **80**, 123527 (2009), 0910.1361.
- [35] The Planck Collaboration, ArXiv Astrophysics e-prints (2006), arXiv:astro-ph/0604069.
- [36] E. Komatsu and D. N. Spergel, *Phys. Rev. D* **63**, 063002 (2001), arXiv:astro-ph/0005036.
- [37] L. Verde, L. Wang, A. F. Heavens, and M. Kamionkowski, *Mon. Not. R. Astron. Soc.* **313**, 141 (2000), arXiv:astro-ph/9906301.
- [38] M. S. Warren, K. Abazajian, D. E. Holz, and L. Teodoro, *Astrophys. J.* **646**, 881 (2006), arXiv:astro-ph/0506395.
- [39] R. K. Sheth, H. J. Mo, and G. Tormen, *Mon. Not. R. Astron. Soc.* **323**, 1 (2001), arXiv:astro-ph/9907024.
- [40] L. Knox, *Phys. Rev. D* **52**, 4307 (1995), arXiv:astro-ph/9504054.
- [41] M. D. Niemack, P. A. R. Ade, J. Aguirre, F. Barrientos, J. A. Beall, J. R. Bond, J. Britton, H. M. Cho, S. Das, M. J. Devlin, et al., in *Society of Photo-Optical Instrumentation Engineers (SPIE) Conference Series* (2010), vol. 7741 of *Society of Photo-Optical Instrumentation Engineers (SPIE) Conference Series*, 1006.5049.
- [42] A. Lewis and A. Challinor, *Phys. Rep.* **429**, 1 (2006), arXiv:astro-ph/0601594.
- [43] W. Hu and T. Okamoto, *Astrophys. J.* **574**, 566 (2002), arXiv:astro-ph/0111606.
- [44] T. Okamoto and W. Hu, *Phys. Rev. D* **67**, 083002 (2003), arXiv:astro-ph/0301031.
- [45] G. M. Bernstein and M. Jarvis, *Astron. J.* **123**, 583 (2002), arXiv:astro-ph/0107431.
- [46] J.-Q. Xia, M. Viel, C. Baccigalupi, G. De Zotti, S. Matarrese, and L. Verde, *Astrophys. J Lett.* **717**, L17 (2010), 1003.3451.
- [47] J.-Q. Xia, A. Bonaldi, C. Baccigalupi, G. De Zotti, S. Matarrese, L. Verde, and M. Viel, *JCAP* **8**, 13 (2010), 1007.1969.
- [48] Y. Takeuchi, K. Ichiki, and T. Matsubara, *Phys. Rev. D* **82**, 023517 (2010), 1005.3492.
- [49] G. M. Bernstein, *Astrophys. J.* **695**, 652 (2009), 0808.3400.

- [50] S. Das, R. de Putter, E. V. Linder, and R. Nakajima, ArXiv e-prints (2011), 1102.5090.
- [51] Z. Ma, W. Hu, and D. Huterer, *Astrophys. J.* **636**, 21 (2006), arXiv:astro-ph/0506614.
- [52] M. Tegmark, A. N. Taylor, and A. F. Heavens, *Astrophys. J.* **480**, 22 (1997), arXiv:astro-ph/9603021.
- [53] J. Dunkley, R. Hlozek, J. Sievers, V. Acquaviva, P. A. R. Ade, P. Aguirre, M. Amiri, J. W. Appel, L. F. Barrientos, E. S. Battistelli, et al., ArXiv e-prints (2010), 1009.0866.
- [54] C. L. Reichardt, P. A. R. Ade, J. J. Bock, J. R. Bond, J. A. Brevik, C. R. Contaldi, M. D. Daub, J. T. Dempsey, J. H. Goldstein, W. L. Holzapfel, et al., *Astrophys. J.* **694**, 1200 (2009), 0801.1491.
- [55] A. Lewis, A. Challinor, and D. Hanson, *JCAP* **3**, 18 (2011), 1101.2234.
- [56] A. Challinor and A. Lewis, *Phys. Rev. D* **84**, 043516 (2011), 1105.5292.
- [57] E. Komatsu, K. M. Smith, J. Dunkley, C. L. Bennett, B. Gold, G. Hinshaw, N. Jarosik, D. Larson, M. R.olta, L. Page, et al., *Astrophys. J Supp.* **192**, 18 (2011), 1001.4538.
- [58] A. Lewis, A. Challinor, and A. Lasenby, *Astrophys. J.* **538**, 473 (2000), arXiv:astro-ph/9911177.
- [59] R. E. Smith, J. A. Peacock, A. Jenkins, S. D. M. White, C. S. Frenk, F. R. Pearce, P. A. Thomas, G. Efstathiou, and H. M. P. Couchman, *Mon. Not. R. Astron. Soc.* **341**, 1311 (2003), arXiv:astro-ph/0207664.
- [60] H. V. Peiris and D. N. Spergel, *Astrophys. J.* **540**, 605 (2000), arXiv:astro-ph/0001393.
- [61] T. Namikawa, T. Okamura, and A. Taruya, *Phys. Rev. D* **83**, 123514 (2011), 1103.1118.
- [62] T. Schwetz, M. Tórtola, and J. W. F. Valle, *New Journal of Physics* **10**, 113011 (2008), 0808.2016.
- [63] M. Maltoni, T. Schwetz, M. Tórtola, and J. W. F. Valle, *New Journal of Physics* **6**, 122 (2004), arXiv:hep-ph/0405172.
- [64] K. Ichiki and M. Takada, ArXiv e-prints (2011), 1108.4688.
- [65] D. Huterer, M. Takada, G. Bernstein, and B. Jain, *Mon. Not. R. Astron. Soc.* **366**, 101 (2006), arXiv:astro-ph/0506030.